



1 **Comparative Analysis of $\mu(I)$ and Voellmy-Type Grain Flow Rheologies in**
2 **Geophysical Mass Flows: Insights from Theoretical and Real Case Studies**

3 Yu Zhuang^{1,2}, Brian W. McArdell³, Perry Bartelt^{1,2}

4 ¹WSL Institute for Snow and Avalanche Research SLF, Davos Dorf, Switzerland

5 ²Climate Change, Extremes and Natural Hazards in Alpine Regions Research Centre CERC

6 ³Swiss Federal Institute for Forest, Snow and Landscape Research WSL, Birmensdorf, Switzerland

7 Corresponding author: Yu Zhuang (yu.zhuang@slf.ch)

8 **Abstract**

9 The experimental-based $\mu(I)$ rheology is now prevalent to describe the movement of gravitational mass
10 flows. Here, we reformulate $\mu(I)$ rheology as a Voellmy-type relationship to illustrate its physical
11 implications. Through one-dimensional block modeling and a real case study, we explore the equivalence
12 between $\mu(I)$ and widely-used Voellmy-type grain flow rheologies. Results indicate that $\mu(I)$
13 rheology utilizes a dimensionless inertial number to mimic contributions of granular
14 temperature/fluctuation energy. In terms of Voellmy, the $\mu(I)$ rheology contains a velocity-dependent
15 turbulent friction coefficient modelling shear thinning behavior. This turbulent friction assumes the
16 production and decay of fluctuation energy are in balance, exhibiting no difference during accelerative
17 and dispositional phases. The constant Coulomb friction coefficient prevents $\mu(I)$ rheology from
18 accurately modeling the dispositional characteristics of actual mass flows. Our results highlight the
19 strengths and limitations of both $\mu(I)$ and Voellmy rheologies, bolstering the theoretical foundation of
20 mass flow modeling while revealing practical engineering challenges.

21 **Keywords:** $\mu(I)$ rheology; Voellmy-Type Grain Flow Rheologies; Geophysical Mass Flows;
22 Avalanche risk assessment



23 **1. Introduction**

24 Creating dependable methods to forecast the runout and deposition characteristics of geophysical mass
25 flows stands as a fundamental challenge in natural hazard research. Long runout mass flows, like debris
26 flows, rock/ice avalanches and snow slides, occur in complex mountain terrain and exhibit an array of
27 complex outcomes depending on their initial material composition and dynamic interactions with the
28 flowing substrate. These mass movements of granular composition exhibit significant mobility, vast
29 energy, and diverse flow patterns, posing challenges for prediction using numerical models (Crosta et al.,
30 2007; Hürlimann et al., 2015; Iverson et al., 2015; Frigo et al., 2021; Shugar et al., 2021). A crucial
31 element for precise modeling of their various behaviors is the development of a universal rheology
32 capable of accurately capturing their granular motion, including long-distance travel, transitions between
33 flow regimes, and eventual deposition.

34 Presently, two primary types of numerical models dominate in engineering practice: discrete
35 element methodologies (Scaringi et al., 2018; Zhao & Crosta, 2018) and continuum approaches, often
36 employing depth-averaged techniques (Hungr & McDougall, 2009; Christen et al., 2010). Discrete
37 approaches simulate particle interactions, incorporating fragmentation processes, thus adeptly portraying
38 the complex behavior of flowing granular materials (Katz et al., 2014; Zhao et al., 2017; Zhuang et al.,
39 2023). Nonetheless, accurately replicating the sheer volume of particles within real geophysical mass
40 flows remains a formidable challenge, constraining their utility for solving large-scale problems due to
41 computational constraints. Conversely, the continuum approaches treat the mass flow as a “granular fluid”
42 consisting of particle ensembles. They utilize a series of differential equations to calculate the flow
43 process, offering high computational efficiency (McDougall & Hungr, 2004; Christen et al., 2010;
44 Mergili et al., 2017). Because existing continuum approaches account for the essential process of ground



45 entrainment (Sovilla & Bartelt, 2002, Bartelt et al., 2018a), frictional heating and phase changes (Valero
46 et al., 2015; Bartelt et al., 2018b), they are somewhat more advanced than discrete element approaches
47 and thus have been widely used to assess mass flow hazard.

48 The Voellmy rheology (Voellmy, 1995) has a long tradition in the hazard mitigation community and
49 is applied to predict the velocity and runout of avalanches and debris flows (Hungri, 1995; Schraml et al.,
50 2015; Aaron et al., 2019; Zhuang et al., 2020). It defines the relationship $\mu(V)=S/N$ as follows:

$$51 \quad \mu(V) = \frac{S}{N} = \mu_s + \frac{v^2}{\xi_0 h} \quad (1)$$

52 where μ_s considers the Coulomb friction at “stopping”, v is the flowing velocity, ξ_0 the “turbulent”
53 friction parameter; h the flowing height. Voellmy considers μ_s to describe the “solid” behavior of the
54 flowing mass, whereas ξ_0 represents the “fluid”-like behavior. Because the Voellmy model is grounded
55 in clear physical principles and involves only two parameters, it is frequently used in hazard mitigation.
56 However, a major issue with the Voellmy model is that the travel resistance of mass flows varies
57 significantly with the flow regime (Gruber and Bartelt, 1998). In the Voellmy model, each flow regime
58 requires a distinct set of calibrated flow parameters; there is no universal parameter set available,
59 rendering the Voellmy approach somewhat makeshift. To address this issue, multiple researchers have
60 suggested incorporating the concept of granular temperature (fluctuation energy R) to accurately model
61 the flow of granular materials across both dense and fluidized flow regimes (Haff, 1983; Jenkins &
62 Savage, 1983; Jenkins & Mancini, 1987; Gubler, 1987; Buser & Bartelt, 2009). This approach involves
63 adding an extra differential equation to account for the generation and dissipation of kinetic energy due
64 to random particle movements (Bartelt et al., 2006). The fluctuation energy arises from shear-work rate
65 \dot{W}_f and decays by dissipative granular interactions (Haff, 1983):

$$66 \quad \frac{dR(t)}{dt} = \alpha \dot{W}_f(t) - \beta(R)R(t) \quad (2)$$



67 where α governs the production and β governs the decay of the fluctuation energy. It is possible to
68 express the friction parameters (μ_s , ξ) as a function of the fluctuation energy, named $\mu(R)$ rheology.

69 Within the Voellmy framework, the $\mu(R)$ rheology has the form (Christen et al., 2010):

$$70 \quad \mu(R) = \mu_s(R) + \frac{v^2}{\xi(R)h} \quad (3)$$

71 where $\mu_s(R) = \mu_s e^{\frac{R(t)}{R_0}}$, $\xi(R) = \xi_0 e^{\frac{R(t)}{R_0}}$, the parameter R_0 scales the fluctuation energy. This $\mu(R)$
72 rheology has the advantage of modeling shear-thinning in avalanche flows, showing a better agreement
73 with observed front velocities and mapped deposition patterns of avalanches than the classic Voellmy
74 approach (Preuth et al., 2010; Bartelt et al., 2012).

75 Recently, the $\mu(I)$ rheology is newly proposed to describe the motion of geophysical flows. It arose
76 directly from the study of small-scale granular experiments (GDR MIDI, 2004; Jop et al., 2006):

$$77 \quad \mu(I) = \frac{s}{N} = \mu_s + \frac{(\mu_2 - \mu_s)}{I_n + 1} \quad (4)$$

78 Similar to Voellmy, the model consists of two parts. The first part consists of the stopping friction μ_s .
79 The second term is controlled by the inertial number I_n which is defined as:

$$80 \quad I_n = \frac{5}{2h} \frac{vd}{\sqrt{g_z h}} \quad (5)$$

81 where d is the granule diameter and g_z the slope perpendicular component of gravity. The model
82 contains two additional constant parameters, I_0 and μ_2 , which can be considered the friction at large
83 I_n . Because of its well-established experimental foundation, the $\mu(I)$ model has become popular in the
84 granular mechanics community and is applied in hazard practice (e.g., Longo et al., 2019; Liu et al.,
85 2022). Although there is broad interest and advocacy for its use, the physical implications of the $\mu(I)$
86 rheology are not completely understood, which restricts its widespread adoption.

87 In this study, we reformulate the $\mu(I)$ rheology as a Voellmy-type relationship. Through one-
88 dimensional block modeling, we investigate the equivalence and difference between the $\mu(I)$ and



89 Voellmy-type grain flow rheologies. A historical case-Piz Cengalo avalanche in Switzerland is further
90 analyzed to exhibit the performance of the $\mu(I)$ rheology. The primary objective of this study is to
91 establish the $\mu(I)$ rheology on a more robust theoretical framework, critically enhancing our
92 understanding of its utility in predicting the dynamics of geophysical mass flows. This endeavor is
93 essential to establish a comparative understanding of different models presently used in natural hazards
94 practice.

95 **2. Method and Data**

96 **2.1 Reformulation of the $\mu(I)$ rheology**

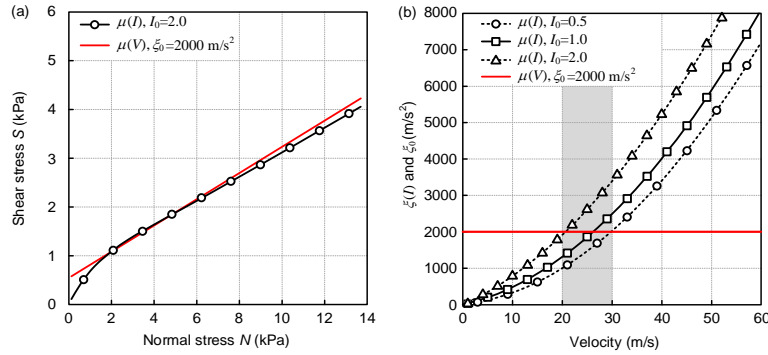
97 The rheological model describes the relationship between the shear stress S to the normal stress N of the
98 flowing mass. The comparison between the $\mu(V)$ and $\mu(I)$ rheologies is for practical applications
99 intuitively made in S vs N space. Here, we vary the flow height (normal stress) and fix the velocity at a
100 specific value to make the comparison, as presented in Fig. 1a. The quantitative and qualitative similarity
101 between the $\mu(V)$ and $\mu(I)$ approaches in S vs N space suggests a mathematical relationship between
102 the two models. In light of this, we have reformulated the $\mu(I)$ rheology using a Voellmy sum:

$$103 \quad \mu(I) = \mu_s + \frac{v^2}{\xi(I)h} \quad (6)$$

104 where $\xi(I)$ characterizes the “turbulent friction” of the $\mu(I)$ model. We find:

$$105 \quad \xi(I) = \frac{v[2I_0h\sqrt{g_2h+5vd}]}{5(\mu_2-\mu_s)d} \quad (7)$$

106 Different from the constant ξ_0 value in the Voellmy, $\xi(I)$ is changing during the flowing process, and
107 is dependent on the flowing velocity and height (Fig. 1b).



108

109 **Figure 1.** $\mu(I)$ vs $\mu(V)$ rheology for typical snow avalanche conditions, $v=20$ m/s and $\rho=300$ kg/m³.
 110 For this example, we take $\mu_s=0.2679=\tan(15^\circ)$ and $\mu_2=0.8391=\tan(40^\circ)$. (a) The curve $I_0=2.0$ plotted
 111 against $\mu(V)$ with $\xi_0=2000$ m/s². Note the strong similarity between the $\mu(I)$ and $\mu(V)$ approaches
 112 in S vs N space. (b) Comparison of the $\mu(I)$ vs $\mu(V)$ rheologies in velocity space. $\xi(I)$ increases with
 113 velocity; $\xi(V)=\xi_0$ is constant. In the shaded region $20\text{m/s} \leq v \leq 30\text{m/s}$, the $\xi(I)$ and $\xi(V)$ values
 114 are similar.

115 2.2 One-dimensional block modeling analysis

116 The turbulent friction coefficient $\xi(I)$ is velocity-dependent. According to Fig. 1, the primary reason
 117 for the similarity of the two results is the selected velocity for the comparison $v=20$ m/s. For velocities
 118 outside this range, the $\xi(I)$ and $\xi(V)=\xi_0$ =constant values differ (Fig. 1b). Therefore, to investigate the
 119 difference between $\mu(I)$ and $\mu(V, R)$, we must study the models over a wide range of velocities typical
 120 for a specific geophysical flow from initiation to runout.

121 For this purpose, we construct a one-dimensional block model. A block of height h and mass m
 122 starts from rest on a steep slope of 35° (release zone). After 30 s the block enters a transition zone of 20° ,
 123 where it begins to decelerate. After 90 s the block enters a flat runout zone and stops. We calculate the
 124 speed and location of the block's center-of-mass; friction is given by $\mu(I)$, $\mu(V)$ and $\mu(R)$. The
 125 governing ordinary differential equations for this model are:

$$126 \quad \frac{dx(t)}{dt} = v(t) \quad (8)$$

$$127 \quad \frac{dv(t)}{dt} = g_x(t) - \mu(I, V, R)g_z(t) \quad (9)$$

128 where $x(t)$ is the flowing distance, $v(t)$ is the flowing velocity, and (g_x, g_z) are the components of



129 gravity acceleration.

130 We consider the motion of the center-of-mass to represent the motion of a granular, geophysical
131 flow. Such simple, one-dimensional sliding block models of avalanche flow have been used extensively
132 to calculate hazard maps (Perla et al., 1980). This approach allows us to compare the $\mu(I)$ and $\mu(V, R)$
133 rheologies in velocity space.

134 2.3 Case study of a historical avalanche

135 According to the reformulation of the $\mu(I)$ rheology, $\xi(I)$ parameter is a function of both flowing height
136 and velocity (Eq. 7), which is heavily dependent on the flowing regime and entrainment process. The
137 one-dimensional block model ignores the above essential features and processes. Therefore, we conduct
138 an analysis of a historical avalanche case: Piz Cengalo avalanche. The Piz Cengalo avalanche occurred
139 on 23th August, 2017 with a released rock volume of $\sim 3 \times 10^6 \text{ m}^3$. The sliding mass entrained the glacial
140 of $6 \times 10^5 \text{ m}^3$ and formed a rock-ice avalanche. This avalanche is well documented with laser scans of
141 release and deposits, providing natural materials to confirm the numerical model (Mergili et al., 2020;
142 Walter et al., 2020). We implement the Voellmy $\mu(V)$, $\mu(I)$ and $\mu(R)$ rheologies into a continuum
143 approach-based model RAMMS (Christen et al., 2010; Bartelt et al., 2018b) to elucidate the performance
144 and limitations of the $\mu(I)$ rheology in calculating the evolution of geophysical mass flows. Detailed
145 information about the well-established RAMMS model can be found in Christen et al. (2010), and Bartelt
146 et al. (2016, 2018b).

147 3. Results

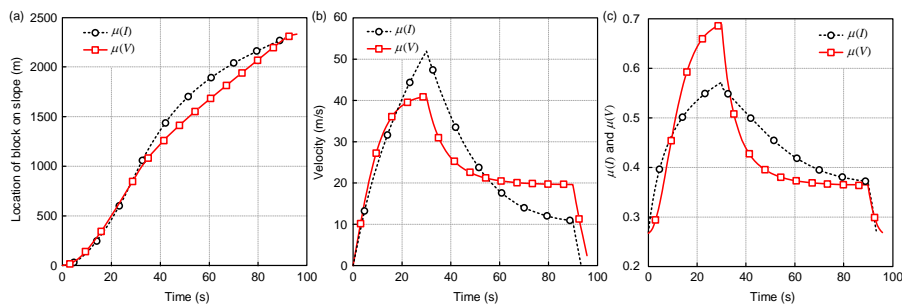
148 3.1 Rheology comparison using the one-dimensional block model

149 (1) The $\mu(I)$ and $\mu(V)$ rheologies in velocity space

150 The direct comparison of $\mu(I)$ and $\mu(V)$ reveals that both models can produce similar runout (Fig. 2a),



151 and velocity (Fig. 2b). However, the $\mu(V)$ approach reaches a smaller peak velocity at the end of the
152 release zone but decelerates less strongly in the transition zone (Fig. 2b). In the end, the velocity at the
153 beginning of the runout zone is higher. This result can also be visualized in the depiction of location
154 through time (Fig. 2a). The Voellmy flow reaches the same runout distance but lags the $\mu(I)$ model
155 along the intermediate transition segment. Of interest is a direct comparison of $\mu(I)$ and $\mu(V)$ through
156 time (Fig. 2c). The $\mu(V)$ with constant ξ_0 reaches larger values (lower velocities) but decreases rapidly
157 during the transition to the flatter 20° slope, falling to values smaller than $\mu(I)$. Both models predict the
158 same μ values as the block enters the flat runout zone. According to Eq. 7, $\xi(I)$ increases with the
159 flowing velocity, indicating a shear-thinning type of behavior and therefore a smaller resistance in the
160 acceleration stage. The general model behavior over the three slope segments can be explained by the
161 fact that the constant ξ_0 value characterizes a mean value within the domain of possible $\xi(I)$ values.
162 Model parameters can be selected such that similar results are obtained; experiments are required to
163 determine which accelerative/decelerative behavior represents the best fit to observations. However,
164 there is a method to bring the two model approaches into equivalence.



165
166 **Figure 2.** The $\mu(I)$ vs $\mu(V)$ rheologies in velocity space. (a) Location of center-of-mass over time. In
167 the transition zone the Voellmy model with constant ξ_0 lags the $\mu(I)$ model. (b) Velocity over time.
168 With a constant ξ_0 the Voellmy model tends to a steady velocity, albeit a lower velocity than $\mu(I)$. At
169 the end of the transition zone, the Voellmy model predicts a higher (steady state) velocity. (c) S/N for
170 $\mu(I)$ and $\mu(V)$. The Voellmy model predicts higher friction before entering the transition zone.
171



172 **(2) The Voellmy grain-flow equivalent to $\mu(I)$: The $\mu(R)$ grain flow rheology**

173 The Voellmy-type $\mu(R)$ rheology is a function of granular temperature/fluctuation energy, which arises
174 from shearing work and decays by dissipative granular interactions. To better compare the $\mu(I)$ and
175 $\mu(R)$ rheologies, we made the Coulomb friction parameter $\mu_s(R)$ a constant but turbulent friction
176 parameter $\xi(R)$ a function of fluctuation energy, so that the two rheologies are in the same Voellmy-
177 type. When we re-solve the ordinary differential equations (Eqs. 8 and 9) with the additional production-
178 decay equation (Eq. 2) and the parameters $\alpha = 0.05$, $\beta = 0.95$, $\xi_0 = 500 \text{ m/s}^2$ and $R_0 = 6 \text{ kJ}$, we find a
179 remarkable duplication of the $\mu(I)$ results, with regard to calculated location (Fig. 3a), velocity (Fig.
180 3b) and calculated $\mu(I)$ and $\mu(R)$ (Fig. 3c). In this comparison the $\mu(I)$ model employed the
181 following parameters, $I_0 = 1.0$, $d = 0.07 \text{ m}$, $\mu_2 = \tan(40^\circ)$ and $\mu_s = \tan(15^\circ)$.

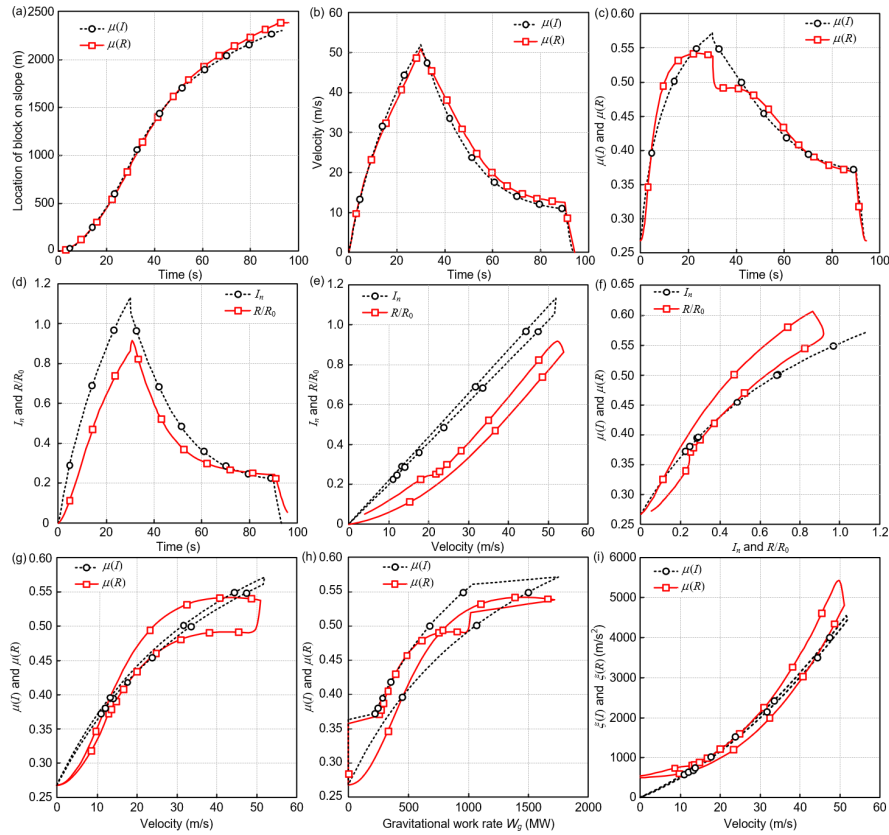
182 These results suggest that the empirical I_n function mimics the production and decay of the
183 granular temperature R . Indeed, there is a strong qualitative similarity between the calculated I_n and
184 R functions. When the two dimensionless parameters I_n and R/R_0 are plotted over time (Fig. 3d) or as
185 a function of the calculated velocity (Fig. 3e) there is both a strong qualitative and quantitative agreement.
186 Because I_n is a pure function of velocity (for a constant height), the calculated friction $\mu(I)$ exhibits
187 no change during the accelerative and decelerative phases of the flow: it ascends and descends on the
188 same path (Fig. 3f). In contrast, because R is a result of a production/decay equation it exhibits a
189 hysteresis (the friction does not follow the same path in the accelerative/decelerative phases of the flow).

190 Hysteresis effects have been observed in experiments with granular materials (Platzer et al., 2004;
191 Bartelt et al., 2007) and grain flows of snow (Platzer et al., 2007, Bartelt et al., 2015). They indicate a
192 process-dependent flow rheology that cannot be described by rheologies with constant flow parameters
193 (e.g., $\mu(V)$). They suggest that the friction must change as the state of the flow changes, for example as



194 the grain flow continuum changes velocity. The correspondence between $\mu(I)$ and $\mu(R)$ models
195 underscores the importance of embracing randomness and temporal evolution in the modeling of granular
196 flows.

197 Both $\mu(I)$ and $\mu(R)$ rheologies exhibit hysteresis in terms of velocity (Fig. 3g) or gravitational
198 work rate (Fig. 3h). Although the $\mu(I)$ friction expressed in terms of I_n exhibits no hysteresis (Fig. 3f),
199 the $\mu(I)$ rheology in terms of velocity and gravitational work rate does. However, this dependency is
200 much more prominent in the $\mu(R)$ -type rheologies because it is governed by two processes-both the
201 production of fluctuation energy and its eventual decay. The $\mu(I)$ approach models the net production,
202 always assuming that the two are in balance. During slope transitions, or other flow states in which
203 production and decay are out-of-balance, this might not be the appropriate description. This is why the
204 most apparent differences between $\mu(I)$ and $\mu(R)$ arise during slope transitions. Despite these
205 differences, however, there is a strong correlation between $\mu(I)$ and $\mu(R)$. For example, when we
206 depict the calculate $\xi(I)$ and $\xi(R)$ function in terms of velocity there is almost a one-to-one agreement
207 in the numerical values (Fig. 3i). The only significant difference is that the $\mu(I)$ rheology predicts an
208 infinite friction ($\xi(I)=0$) at the velocity of zero, whereas the $\mu(R)$ approach predicts some finite value
209 (in this case when $R=0$, $\xi(R)=\xi_0$).



210
 211 **Figure 3.** Comparison between the $\mu(I)$ vs $\mu(R)$ rheologies. (a)-(c) show the calculated location of
 212 center-of-mass, velocity and friction of the two rheologies. (d)-(e) Comparison between I_n and R/R_0
 213 over time and flow velocity. (f) Calculated friction $\mu(I)$ vs $\mu(R)$ as a function of I_n and R/R_0 . (g)-(h)
 214 Calculated $\mu(I)$ vs $\mu(R)$ as a function of the velocity and gravitational work rate. (i) Comparison
 215 between $\xi(I)$ (Eq. 7) and $\xi(R)$.

216 3.2 Rheology comparison using a real case study: Piz Cengalo avalanche

217 We apply the $\mu(I)$, $\mu(V)$, and $\mu(R)$ rheologies to calculate the dynamics of the Piz Cengalo avalanche.

218 Modeling parameters are presented in Fig. 4. The $\mu(R)$ parameters are empirical values, which arise

219 from practical experience in Switzerland and have been widely used in rock-ice avalanche research. Here,

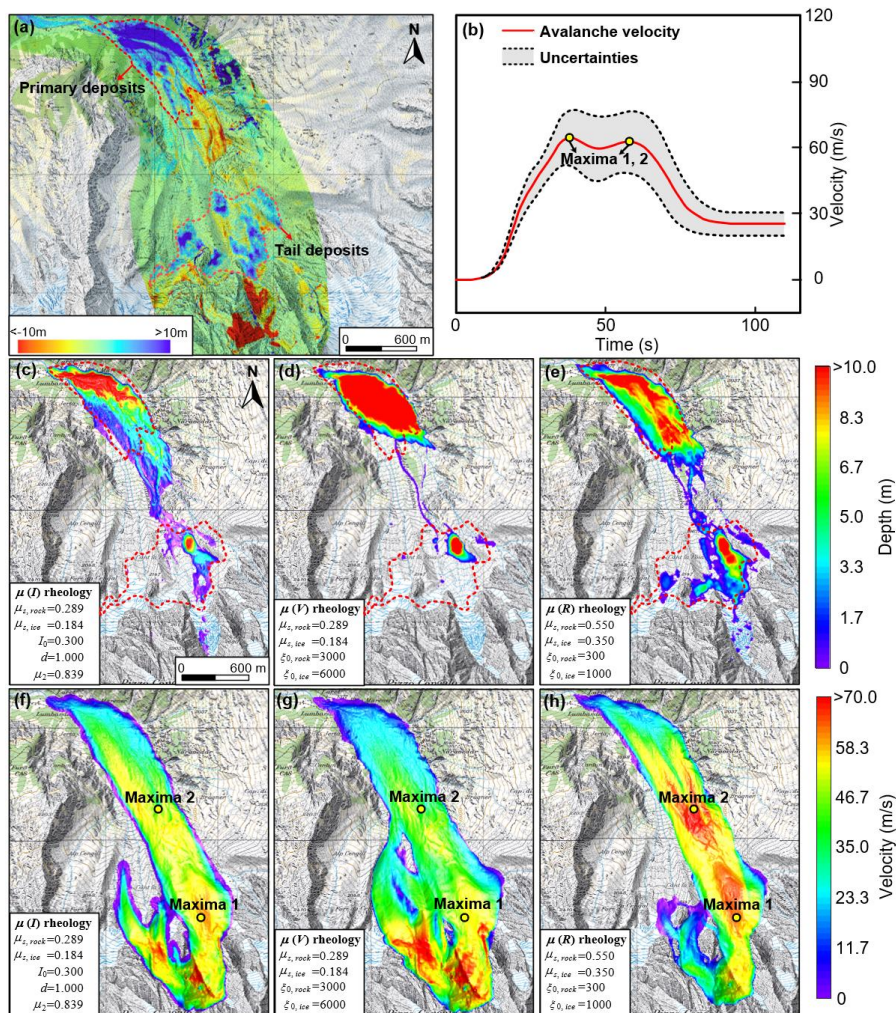
220 the Coulomb and turbulent friction coefficients $\langle \mu_s(R), \xi(R) \rangle$ are both functions of the fluctuation

221 energy. In the $\mu(I)$ rheology, $I_0=0.3$ is a typical value from Pouliquen & Forterre (2002), Forterre &

222 Pouliquen (2003), and Jop et al. (2006), $d=1.0$ m and $\mu_2=\tan(40^\circ)=0.839$ arise from field investigations



223 of particle size and deposit distribution. The μ_s value and parameters in the $\mu(V)$ rheology are
 224 determined from inversion analysis that the calculated avalanche runout matches the actual condition.
 225 For ease of comparison, the same Coulomb friction coefficients are applied in the $\mu(I)$ and $\mu(V)$
 226 rheologies.



227
 228 **Figure 4.** Rheology comparison with the Piz Cengalo avalanche. (a) Deposit structure arises from the
 229 laser scans. (b) Seismic signal analysis of the avalanche velocity, derived by Walter et al. 2020. (c)-(e)
 230 Modeled avalanche deposits with different rheologies. (4) Modeled avalanche velocity with different
 231 rheologies. Two maxima represent the locations derived by seismic signal analysis.

232 Modeling results of all three rheologies exhibit satisfactory runout distance, but there are deviations



233 in the calculated deposit structure and avalanche velocity. Laser scans indicate two deposit areas of the
234 Piz Cengalo avalanche (Fig. 4a): a primary deposit area of $\sim 2 \times 10^5$ m² at the mountain toe (1350-1450
235 m a.s.l.) and tail deposits spread on the steep slope (2000 m-2250 m a.s.l.). Both $\mu(I)$ and $\mu(V)$ models
236 make a deposit anomaly at the mountain toe (Fig. 4 c and d), exceeding the measurements considerably.
237 Very few deposits remained on the steep slope, resulting in significantly smaller accumulation area and
238 thickness compared to the actual condition. Conversely, modeling deposits of the $\mu(R)$ model exhibits
239 a reasonable deposit structure, whether in the primary deposit area or on the steep slope (Fig. 4e). To
240 align the calculated avalanche runout with the actual condition, small Coulomb friction μ_s , which is
241 dominant when the avalanche comes close to stopping, is applied in the $\mu(I)$ and $\mu(V)$ models. This
242 modification dictates the final runout accumulation, leading to deposits primarily concentrated on areas
243 with gentle slopes, while leaving smaller deposits on steeper inclines. According to the seismic signal
244 analysis (Fig. 4b, Walter et al., 2020), the Piz Cengalo avalanche has a duration of ~ 100 s and a maximum
245 velocity of 64 m/s. There are two avalanche velocity maxima: the first reaches when the avalanche leaves
246 the steep glacier portion, and the second occurs behind the steep terrain step in the central runout area.
247 The mean velocity between the two maxima is 40-60 m/s. The analysis comparing modeled avalanche
248 velocities and seismic signals indicates that the $\mu(R)$ rheology outperforms others in terms of peak
249 values and velocity evolution, as shown in Fig. 4h. Seismic signal analysis, representing the average
250 velocity of the mass center, explains why a slightly higher peak velocity is observed in the modeling
251 results. In contrast, the $\mu(I)$ and $\mu(V)$ rheologies display higher velocities downstream from the
252 source area but show reduced velocities in the transition and deposition areas, deviating from actual
253 conditions as depicted in Figs. 4f and 4g. The small Coulomb friction μ_s and high ξ_0 value impart the
254 avalanche with high mobility in the initial stage. This result is also visualized in the modeled deposit



255 distribution that very few materials are deposited on the steep slope.

256 **4. Discussion and Implications**

257 With this contribution, we strengthen the theoretical foundation of the $\mu(I)$ rheology. It has an
258 equivalence with the Voellmy-type grain flow rheologies, which are composed of a Coulomb stopping
259 friction and a turbulent friction that controls the flow velocity. Compared with the classic $\mu(V)$ rheology
260 of constant friction parameters, an advantage of the $\mu(I)$ rheology is to define the turbulent friction
261 parameter $\xi(I)$ as a function of flowing velocity and height (using inertial number I_n). This modification
262 incorporates the shear-thinning behavior (Hu et al., 2022) and the impact of volume (where increased
263 normal stress results in a reduced friction coefficient, see Heim, 1932; Wang et al., 2018), capturing key
264 characteristics of these phenomena. With the help of grain flow theory (Haff, 1983, Jenkins & Savage,
265 1983; Buser & Bartelt, 2009), we find the contribution of I_n attributes to its empirical representation of
266 the granular temperature/fluctuation energy R . However, the inertial number I_n is just a function of
267 flowing velocity, assuming the production and decay of the fluctuation energy are in balance. The $\mu(I)$
268 rheology, therefore, exhibits no change during the acceleration and deceleration process, leading to the
269 deviation of calculated velocity for real case studies.

270 Though the $\mu(I)$ rheology demonstrates an improvement over the classic $\mu(V)$ rheology, it has a
271 critical flaw in ignoring the contribution of fluctuation energy to the Coulomb friction coefficient μ_s . In
272 the $\mu(I)$ rheology, the constant μ_s value makes the sliding mass stop on a single slope angle
273 ($\arctan(\mu_s)$). Consequently, the modeled deposits of the Piz Cengalo avalanche concentrate at the
274 mountain toe, with very few materials deposited on the steep slope. Considering that avalanche deposits
275 in real-world scenarios often cover a broad area with varying thicknesses, using a constant μ_s value is
276 unlikely to yield an accurate representation of the deposit structure.



277 A significant challenge in landslide risk assessment is to establish reliable numerical parameters,
278 highlighting a limitation in both the $\mu(I)$ and classic $\mu(V)$ rheologies: the reliance on input parameters
279 derived from inversion analysis (Zhao et al., 2024). Although the $\mu(I)$ rheology is based on
280 experimental data, relevant experiments are limited, and the test materials used are predominantly glass
281 beads (Fotterre & Pouliquen, 2003; Jop et al., 2006). To date, no large-scale experiments have been
282 conducted on geophysical mass flows, to our knowledge. Considering the substantial differences in
283 properties among materials in the flowing mass, such as rock, ice, snow, and water, it proves highly
284 challenging to accurately characterize avalanche motion using a uniform surrogate material with different
285 properties, such as glass. Additionally, the dynamics of avalanches are greatly influenced by the flow
286 regime and topography, indicating that avalanches composed of the same material can display varied
287 runout lengths and deposit patterns under different conditions.

288 This phenomenon further complicates the task of selecting appropriate model parameters. In this
289 study, to achieve a satisfactory runout of the Piz Cengalo avalanche, small μ_s values arise from
290 inversion analysis are applied for the calculation of $\mu(I)$ and $\mu(V)$ models. We admit that model
291 parameters can be calibrated such that realistic runout is obtained, but these site-specifically calibrated
292 parameters limit the engineering application of the model, particularly when conducting risk assessments
293 of potential avalanches. The existing $\mu(R)$ model offers a possible solution (Christen et al., 2010;
294 Bartelt et al., 2011). By defining the Coulomb stopping friction and turbulent friction parameters as
295 functions of fluctuation energy, we can characterize the effects of flow regime and topography changes
296 on the friction of landslides (Preuth et al., 2010). Using a group of empirical parameters, which represent
297 the material properties of rock and ice, realistic deposit structure and velocity evolution can be obtained.
298 Because R represents the energy associated with random particle motions, it introduces an element of



299 stochasticity into avalanche modelling. Clearly, it is impossible to precisely determine the position of
300 every individual particle in an avalanche, contrary to what Discrete Element Modeling (DEM) might
301 imply. Nonetheless, the behavior of the granular ensemble seems to be directed by a production/decay
302 equation, which, even when estimated approximately, can impart a discernible trajectory to the avalanche
303 process and deposition dynamic, thereby enhancing predictive accuracy of numerical models.

304 These insights have practical implications for improving geophysical flow models, offering a more
305 comprehensive understanding of flow behavior and its dependence on factors such as velocity, terrain
306 features, and material properties. As we continue to refine our models, we move closer to more accurate
307 assessments and mitigation of geophysical hazards.

308 **Data availability**

309 No data sets were used in this article.

310 **Author contribution**

311 Yu Zhuang did the numerical work and wrote the manuscript with contributions from all co-authors.

312 Perry Bartelt designed the work, did the calculation and wrote the manuscript. Brian W. McArdell edited
313 the manuscript.

314 **Declaration of competing interest**

315 The authors declare that they have no known competing financial interests or personal relationships that
316 could have appeared to influence the work reported in this paper.

317 **Acknowledgments**

318 This study is supported by the RAMMS project.

319 **References**

320 Aaron, J., McDougall, S., and Nolde, N.: Two methodologies to calibrate landslide runout models,



- 321 Landslides, 16(5), 907-920, 2019.
- 322 Bartelt, P., Buser, O., and Platzler, K.: Fluctuation-dissipation relations for granular snow avalanches,
323 *Journal of Glaciology*, 52(179), 631-643, 2006.
- 324 Bartelt, P., Buser, O., and Platzler, K.: Starving avalanches: frictional mechanisms at the tails of finite-
325 sized mass movements, *Geophysical Research Letters*, 34(20), 1-6, 2007.
- 326 Bartelt, P., Meier, L., and Buser, O.: Snow avalanche flow-regime transitions induced by mass and
327 random kinetic energy fluxes, *Annals of Glaciology*, 52(58), 159-164, 2011
- 328 Bartelt, P., Bühler, Y., Buser, O., Christen, M., and Meier, L.: Modeling mass-dependent flow regime
329 transitions to predict the stopping and depositional behavior of snow avalanches, *Journal of*
330 *Geophysical Research*, 117, F01015, 2012.
- 331 Bartelt, P., Vera Valero, C., Feistl, T., Christen, M., Bühler, Y., and Buser, O.: Modelling cohesion in snow
332 avalanche flow, *Journal of Glaciology*, 61(229), 837-850, 2015.
- 333 Bartelt, P., Christen, M., Bühler, Y., Caviezel, A., and Buser, O.: Snow entrainment: Avalanche interaction
334 with an erodible substrate, *Proceedings, International Snow Science Workshop*, 716-720, 2018a.
- 335 Bartelt, P., Christen, M., Bühler, Y., and Buser, O.: Thermomechanical modelling of rock avalanches with
336 debris, ice and snow entrainment, *Numerical Methods in Geotechnical Engineering*, IX, 1047-1054,
337 2018b.
- 338 Buser, O., and Bartelt, P.: Production and decay of random kinetic energy in granular snow avalanches,
339 *Journal of Glaciology*, 55, 3-12, 2009.
- 340 Christen, M., Kowalski, J., and Bartelt, P.: RAMMS: Numerical simulation of dense snow avalanches in
341 three-dimensional terrain, *Cold Regions Science and Technology*, 63(1-2), 1-14, 2010.
- 342 Crosta, G. B., Frattini, P., & Fusi, N.: Fragmentation in the Val Pola rock avalanche, Italian Alps, *Journal*



- 343 of Geophysical Research: Earth Surface, 112(F1), F01006, 2007.
- 344 Forterre, Y., and Pouliquen, O.: Long-surface-wave instability in dense granular flows, *Journal of Fluid*
345 *Mechanics*, 486, 21-50, 2003.
- 346 Frigo, B., Bartelt, P., Chiaia, B., Chiambretti, I., and Maggioni, M.: A reverse dynamical investigation of
347 the catastrophic wood-snow avalanche of 18 January 2017 at Rigopiano, Gran Sasso National Park,
348 Italy, *International Journal of Disaster Risk Science*, 12, 40-55, 2021.
- 349 GDR, MiD.: On dense granular flows, *The European Physical Journal E*, 14, 341-365, 2004.
- 350 Gruber, U., and Bartelt, P.: Avalanche hazard mapping using numerical Voellmy-fluid models, 1998.
- 351 Gubler, H.: Measurements and modelling of snow avalanche speeds, *IAHS Publ. 162 (Symposium at*
352 *Davos 1986-Avalanche Formation, Movement and Effects)*, 405-420, 1987.
- 353 Haff, P. K.: Grain flow as a fluid-mechanical phenomenon, *Journal of Fluid Mechanics*, 134, 401-430,
354 1983.
- 355 Heim, A.: Bergsturz und Menschenleben. *Beiblatt zur Vierteljahrsschrift der Naturforschenden*
356 *Gesellschaft Zürich*, 20, 217: 1932
- 357 Hu, W., Li, Y., Xu, Q., Huang, R. Q., McSaveney, M., Wang, G. H., Fan, Y., Wasowski, J., and Zheng, Y.
358 S.: Flowslide High Fluidity Induced by Shear Thinning, *Journal of Geophysical Research: Solid*
359 *Earth*, 127, e2022JB024615, 2022.
- 360 Hungr, O.: A model for the runout analysis of rapid flow slides, debris flows, and avalanches, *Canadian*
361 *Geotechnical Journal*, 32(4), 610-623, 1995.
- 362 Hungr, O., and McDougall, S.: Two numerical models for landslide dynamic analysis. *Computers &*
363 *Geosciences*, 35(5), 978-992, 2009.
- 364 Hürlimann, M., McArdeell, B. W., & Rickli C.: Field and laboratory analysis of the runout characteristics



- 365 of hillslope debris flows in Switzerland, *Geomorphology*, 232, 20-32, 2015.
- 366 Iverson, R. M., George, D. L., Allstadt, K., Reid, M. E., Collins, B. D., Vallance, J. W., Schilling, S. P.,
367 Godt, J. W., Cannon, C. M., Magirl, C. S., Baum, R. L., Coe, J. A., Schulz, W. H., and Bower, J. B.:
368 Landslide mobility and hazards: implications of the 2014 Oso disaster, *Earth and Planetary Science*
369 *Letters*, 412, 197-208, 2015.
- 370 Jenkins, J. T., and Savage, S. B.: A theory for the rapid flow of identical, smooth, nearly elastic particles.
371 *Journal of Fluid Mechanics*, 136, 186-202, 1983.
- 372 Jenkins, J. T., and Mancini, F.: Plane flows of a dense, binary mixture of smooth, nearly elastic circular
373 disks, *Journal of Applied Mechanics*, 54(1), 27-34, 1987
- 374 Jop, P., Forterre, Y., and Pouliquen, O.: A constitutive law for dense granular flows, *Nature*, 441(7094),
375 727-730, 2006.
- 376 Katz, O., Morgan J. K., Aharonov, E., and Dugan, B.: Controls on the size and geometry of landslides:
377 Insights from discrete element numerical simulations, *Geomorphology*, 220, 104-113, 2014.
- 378 Liu, Z., Fei, J., and Jie, Y.: Including μ (I) rheology in three-dimensional Navier-Stokes-governed
379 dynamic model for natural avalanches, *Powder Technology*, 396, 406-432, 2022.
- 380 Longo, A., Pastor, M., Sanavia, L., Manzanal, D., Martin Stickle, M., Lin, C., Yague, A., and Tayyebi,
381 S.M.: A depth average SPH model including μ (I) rheology and crushing for rock avalanches,
382 *International Journal for Numerical and Analytical Methods in Geomechanics*, 43(5), 833-857, 2019.
- 383 McDougall, S., and Hungr, O.: A model for the analysis of rapid landslide motion across three-
384 dimensional terrain, *Canadian Geotechnical Journal*, 41(6), 1084-1097, 2004.
- 385 Mergili, M., Fischer, J. T., Krenn, J., and Pudasaini, S. P.: r.avaflow v1, an advanced open-source
386 computational framework for the propagation and interaction of two-phase mass flow, *Geoscientific*



- 387 Model Development, 10, 553-569, 2017.
- 388 Mergili, M., Jaboyedoff, M., Pullarello, J., and Pudasaini, S. P.: Back calculation of the 2017 Piz
389 Cengalo-Bondo landslide cascade with r.avaflow: what we can do and what we can learn, Natural
390 Hazards and Earth System Sciences, 20, 505-520, 2020.
- 391 Perla, R., Cheng, T. T., and McClung, M. D.M.: A Two-Parameter Model of Snow-Avalanche Motion,
392 Journal of Glaciology, 26, 197-207, 1980
- 393 Platzer, K. M., Margreth, S., and Bartelt, P.: Granular flow experiments to investigate dynamic avalanche
394 forces for snow shed design. In P. Bartelt, E. Adams, M. Christen, R. Sack, & A. Sato (Eds.), Snow
395 engineering V, Proceedings of the fifth international conference on snow engineering, 5-8 July 2004,
396 Davos, Switzerland (pp. 363-370), 2004.
- 397 Platzer, K., Bartelt, P., and Kern, M.: Measurements of dense snow avalanche basal shear to normal stress
398 ratios (S/N), Geophysical Research Letters, 34(7), L07501, 2007.
- 399 Pouliquen, O., and Forterre, Y.: Friction law for dense granular flows: application to the motion of a mass
400 down a rough inclined plane, Journal of fluid mechanics, 453, 133-151, 2002.
- 401 Preuth, T., Bartelt, P., Korup, O., and Mcardell, B. W.: A random kinetic energy model for rock
402 avalanches: Eight case studies. Journal of Geophysical Research: Earth Surface, 115, F03036, 2010.
- 403 Scaringi, G., Fan, X. M., Xu, Q., Liu, C., Ouyang, C. J., Domènech, G., Yang, F., and Dai, L. X.: Some
404 considerations on the use of numerical methods to simulate past landslides and possible new failures:
405 the case of the recent Xinmo landslide (Sichuan, China), Landslides, 15, 1359-1375, 2018
- 406 Schraml, K., Thomschitz, B., Mcardell, B. W., Graf, C., and Kaitna, R.: Modeling debris-flow runout
407 patterns on two alpine fans with different dynamic simulation models, Natural Hazards and Earth
408 System Science, 15(7), 1483-1492, 2015.



- 409 Shugar, D. H., et al.: A massive rock and ice avalanche caused the 2021 disaster at Chamoli, Indian
410 Himalaya. *Science*, 373, 300-306, 2021.
- 411 Sovilla, B., and Bartelt, P.: Observations and modelling of snow avalanche entrainment. *Natural Hazards
412 and Earth System Sciences*, 2(3/4), 169-179, 2002.
- 413 Valero, C. V., Jones, K. W., Bühler, Y., & Bartelt, P.: Release temperature, snow-cover entrainment and
414 the thermal flow regime of snow avalanches, *Journal of Glaciology*, 61(225), 173-184, 2015.
- 415 Voellmy, A.: Über die zerstörungskraft von lawinen, *Bauzeitung*, 73, 159-165, 1955.
- 416 Walter, F., Amann, F., Kos, A., Kos, A., Kenner, R., Phillips, M., Preux, A., Huss, M., Tognacca, C.,
417 Clinton, J., Diehl, T., and Bonanomi, Y.: Direct observations of a three million cubic meter rock-
418 slope collapse with almost immediate initiation of ensuing debris flows, *Geomorphology*, 351,
419 106933, 2020.
- 420 Wang, Y. F., Dong, J. J., and Cheng, Q. G.: Normal Stress-Dependent Frictional Weakening of Large
421 Rock Avalanche Basal Facies: Implications for the Rock Avalanche Volume Effect, *Journal of
422 Geophysical Research: Solid Earth*, 123, 3270-3282, 2018.
- 423 Zhao, S. X., He, S. M., Li, X. P., Scaringi, G., Liu, Y., and Deng, Y.: Investigating the dynamic process
424 of a rock avalanche through an MLS-MPM simulation incorporated with a nonlocal $\mu(I)$ rheology
425 model, *Landslides*, 2024. Doi: 10.1007/s10346-024-02244-6
- 426 Zhao, T., Crosta, G. B., Utili, S., and De Blasio, F. V.: Investigation of rock fragmentation during rockfalls
427 and rock avalanches via 3-D discrete element analyses, *Journal of Geophysical Research: Earth
428 Surface*, 122(3), 678-695, 2017.
- 429 Zhao, T., and Crosta, G. B.: On the dynamic fragmentation and lubrication of coseismic landslides.
430 *Journal of Geophysical Research: Solid Earth*, 123,9914-9932, 2018.



- 431 Zhuang, Y., Yin, Y., Xing, A., and Jin, K.: Combined numerical investigation of the Yigong rock slide-
432 debris avalanche and subsequent dam-break flood propagation in Tibet, China, *Landslides*, 17,
433 2217-2229, 2020.
- 434 Zhuang, Y., Xu, Q., Xing, A. G., Bilal, M., and Gnyawali, K. R.: Catastrophic air blasts triggered by large
435 ice/rock avalanches. *Landslides*, 20, 53-64, 2023.